PAPER

Tapered curved-beam hinges for electret-based vibration energy harvesting devices

To cite this article: Dooyoung Hah 2024 *Eng. Res. Express* **6** 045365

Engineering Research Express

PAPER

Tapered curved-beam hinges for electret-based vibration energy harvesting devices

RECEIVED
9 September 2024

REVISED
19 November 2024

ACCEPTED FOR PUBLICATION
3 December 2024

PUBLISHED
24 December 2024

Dooyoung Hah

Abdullah Gül University, Sumer Kampusu, Barbaros Mah., Kayseri 38030, Türkiye

E-mail: dooyoung.hah@agu.edu.tr

Keywords: energy harvester, vibration, nonlinear spring, curved beams, electret, renewable energy

Abstract

Interest in vibration energy harvesting have been growing recently for various applications. One of the major development goals for vibration energy harvesters has been improvement in energy conversion efficiency. To pursue that goal, one of the main approaches has been to broaden the spectra of harvesters. Employment of nonlinear springs, such as curved-beam hinges, has proven to be effective for that purpose. The main contribution of the current study is to introduce a lateral taper to the curved beam so as to further optimize the harvester performances. Via numerical analysis by using stochastic differential equations, the study shows that at 0.05*g* of vibration strength, tapered curved-beam hinges can result in higher electric power output than the non-tapered ones. Deformation-induced stress was taken into consideration as well, in reference to the fracture strength of the material (single-crystal silicon). At lower vibration strength (0.02*g*), spring nonlinearity becomes weaker, and as a result, the narrowest curved-beam hinge produces the highest output power. Overall, the current study demonstrates that tapering of the curved beam can be a useful addition in the vibration energy harvester design.

1. Introduction

Energy harvesting has become one of the key research topics in recent decades. Abundance of sources in environment makes vibration energy scavenging highly attractive as one of the promising candidates [1–4]. Various application fields can benefit from vibration energy harvesters (VEHs), such as wireless sensor networks, internet of things, infrastructure monitoring, implantable medical devices, and so on. One of the important aspects in VEHs is their spectral characteristics. More often than not, vibration sources found in environment have broad, random, and time-varying spectra. To increase energy harvesting efficiencies from the sources of this nature, it is imperative to reduce spectral differences between VEHs and sources [2–4]. A variety of methods have been attempted so far to broaden spectral responses of VEHs. Those methods include Duffing oscillators [5–7], multi degree-of-freedom structures [8–10], an array of single degree-of-freedom structures [11, 12], nonlinear springs, and so on. Among these methods, nonlinear springs are particularly interesting for the applications with limited spaces.

One of the simplest forms a nonlinear spring can have is a straight clamped-clamped beam, which can be modeled as a Duffing oscillator [13]. A Duffing oscillator exhibits third-order nonlinearity (without a second order term). It has been shown that this nonlinearity can broaden frequency response of an energy harvester [14]. Nonlinearity of a clamped-clamped beam can be further strengthened by adding an initial curve to it, which makes it a Duffing-Holmes oscillator [15–22]. Various shapes, such as chevron [15], sinusoidal [16–19], M- [20, 21], crab-leg [22], etc, have been attempted as initial curves. Mollik *et al* [13] used a genetic algorithm to optimize a beam shape for specific nonlinear responses. All of those curve shapes were predetermined at the design stage, i.e. by layout. There also have been reports of curved-beams formed by compression [23–26], which is not quite easy to handle at micro-scale. A Duffing-Holmes oscillator has all three terms (linear, quadratic & cubic) of spring constants as nonzero. This type of oscillator can show interesting behaviors, such as

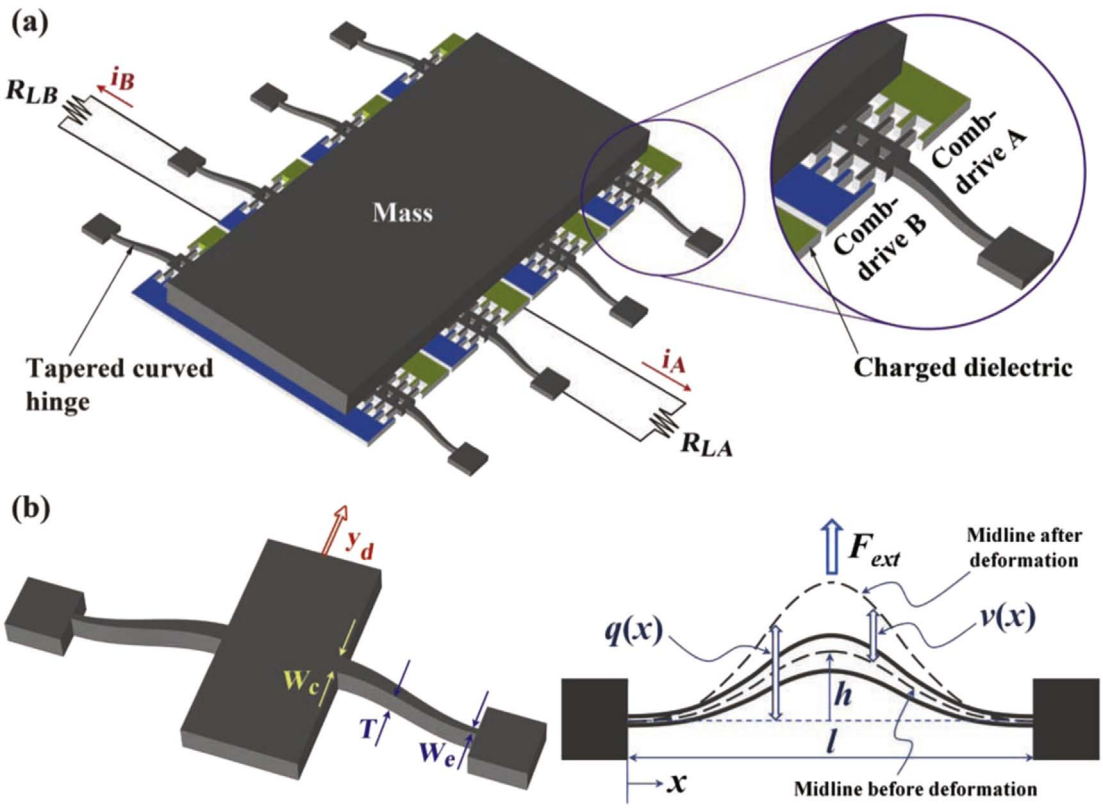

Figure 1. Sketches of the proposed device. (a) An energy harvester. External loads (R_{LA} and R_{LB}) are also shown. (b) Tapered curved-beam hinges; (left) parts between hinges simplified as a block, y_d: beam center displacement; (right) parts between hinges omitted.

snap through and bistability. It has been demonstrated that employment of curved clamped-clamped beam hinges can broaden power spectra of VEHs and increase the harvested power outputs [19].

Design of an electret-based energy harvester is a complex problem that involves several nonlinear aspects. Therefore, it is essential to examine various design parameters. An initial curve height of a beam is one of the key design parameters that influence the energy harvesting performance [19]. By adjusting an initial curve height, one can vary the ratios between a linear spring constant and nonlinear spring constants. A lateral taper (in beam width direction) is another design parameter worthy of investigation without imposing additional fabrication challenge, and this is the main contribution of the current study. Introducing a beam taper can also modify the ratios between a linear term and nonlinear terms of the spring constants so that VEH device performances can be further optimized. In addition, the maximum stress levels a tapered curved-hinge experiences during operation will be investigated as well to explore the practicality of various designs. It will be shown that VEHs with tapered curved-beam hinges can outperform those with non-tapered curved-beam hinges at a certain vibration strength when both power outputs and the maximum stress levels are considered.

This paper is organized as follows. First, the device model will be described in section 2, including analytical derivation and numerical simulation to obtain spring constants of tapered curved-beam hinges. These spring constants will be used in the main analysis. Various transduction mechanisms have been utilized in VEHs, such as electrostatic, electromagnetic, piezoelectric, triboelectric, and so on. Among them, an electrostatic one, more specifically a comb-drive electret [27–30], is the subject of current study. Section 2 will also explain the analysis method based on stochastic differential equations. Section 3 will present the results including power outputs, power spectral densities, and deformation-induced stresses. Finally, discussion and conclusion will be given in section 4.

2. Device model and analysis method

A sketch of the device under consideration is illustrated in figure 1(a). The device configuration loosely follows that of a VEH developed by Honma *et al* [27]. The main feature of their device is a balanced configuration. Such a configuration is advantageous, especially at low vibration strength, with electrostatic forces by two combs canceling each other. When acting alone, electrostatic force hinders free motion of a mass. Also in their device,

comb fingers are coated with charged dielectric on the sidewalls, fabricated by oxidation with doping, which is followed by polarization. These processes make the comb structures electrets. The main deviation of a VEH in current study from the one in [27] is incorporation of curved-beam hinges instead of straight folded-beam springs. As a mass (attached to the moving part of comb-drives) moves in response to external vibration, engagements of the comb fingers change, resulting in charge redistribution. This charge redistribution becomes sources of electric current (i_A & i_B) generation through loads (R_{LA} & R_{LB}, see figure 1(a)). Force induced by the mass movement (F_{ext}) is balanced with restoring force of the hinges (F_r) and electrostatic force of the comb-drives.

2.1. Tapered curved-beam hinge - theory

First, relationships between spring constants of a tapered curved-beam hinge and its geometries will be analytically derived by examining its elastic energy. In the following subsection, it will be compared to the results obtained from numerical analysis.

Figure 1(b) shows the details of a tapered curved-beam hinge. The predetermined shape of a beam mid-plane (marked as a midline before deformation) is according to the fundamental mode $\psi(x)$ of beam deformation as follows.

$$h\psi(x) = \frac{h}{2}\left(1 - \cos\frac{2\pi x}{l}\right),\ x \in [0,\ l] \tag{1}$$

where h and l are a height and a length of the beam, respectively. A linear taper is considered in the beam width $W_b(x)$ as follows.

$$W_b(x) = W_e + (W_c - W_e)\frac{2x}{l} = W_e + \frac{4W_d}{l}x,\ x \in \left[0,\ \frac{l}{2}\right] \tag{2}$$

where W_c and W_e are beam widths at the center and at the edge, respectively. W_d is defined as $(W_c - W_e)/2$, which represents the beam taper rate. When the beam is deformed in response to applied force, its shape contains a number of modes. By using the Galerkin method with one-mode approximation, the beam deflection $v(x,\ t)$ and the beam shape after deformation $q(x,\ t)$ can be expressed as [31, 32],

$$q(x,\ t) = h\psi(x) + v(x,\ t) = h\psi(x) + y_d(t)\psi(x) \tag{3}$$

where y_d is the beam center displacement and t is time.

When the beam is deformed, potential energies from three different origins are stored in the beam: (1) U_b from bending, (2) U_p from axial load and (3) U_m from mid-plane stretching. U_b can be found as [31],

$$\begin{aligned} U_b &= 2\int_0^{\frac{l}{2}} \tfrac{1}{2}EI(x)\left(\tfrac{\partial^2 v}{\partial x^2}\right)dx \\ &= \tfrac{\pi^4 E T y_d^2}{6l^3}\left[\left(1 + \tfrac{3}{\pi}\right)W_d^3 + \left(2 + \tfrac{3}{\pi^2}\right)W_d^2 W_e + \tfrac{3}{2}W_d W_e^2 + \tfrac{1}{2}W_e^3\right] \end{aligned} \tag{4}$$

where E, $I(x)$ and T are Young's modulus, moment of inertia, and a thickness of the beam, respectively. U_p caused by an axial load P can be expressed as [31],

$$U_p = -2\int_0^{\frac{l}{2}} \frac{1}{2}P\left(\frac{\partial q}{\partial x}\right)^2 dx = -\frac{\pi^4 ET}{16l^3}h^2(h + y_d)^2(W_e + W_d). \tag{5}$$

Mid-plane stretching Δ and axial force S induced by it can be expressed as [31],

$$\Delta = 2\int_0^{\frac{l}{2}} \frac{1}{2}\left(\frac{\partial q}{\partial x}\right)^2 dx = \frac{\pi^4}{4l}(h + y_d)^2 \tag{6}$$

$$S = 2\frac{E}{l}\int_0^{\frac{l}{2}} \frac{1}{2}A(x)\left(\frac{\partial q}{\partial x}\right)^2 dx = \frac{\pi^2 ET}{4l^2}(h + y_d)^2(W_e + W_d) \tag{7}$$

where $A(x)$ is a cross-section area of the beam. Then, potential energy U_m due to mid-plane stretching can be found as [33],

$$U_m = \frac{1}{2}S\Delta = \frac{\pi^4 ET}{32l^3}(h + y_d)^4(W_e + W_d). \tag{8}$$

Mechanical restoring force of the beam, F_r can be derived by differentiating the total potential energy U with respect to beam center displacement y_d [34].

$$F_r(y_d) = \frac{\partial U}{\partial y_d} = \frac{\partial(U_b + U_p + U_m)}{\partial y_d} = k_1 y_d + k_2 y_d^2 + k_3 y_d^3, \tag{9}$$

and the spring constants (k_1: linear, k_2: quadratic & k_3: cubic) are found as

$$k_1 = \frac{\pi^4 ET}{12l^3}\left[2W_a^2 + \left(2 + \frac{12}{\pi^2}\right)W_d^2 + 3h^2\right]W_a \tag{10a}$$

$$k_2 = \frac{3\pi^4 ET}{8l^3}hW_a \tag{10b}$$

$$k_3 = \frac{\pi^4 ET}{8l^3}W_a \tag{10c}$$

where W_a is defined as $(W_c + W_e)/2$, i.e. an average beam width. From equations (10a–10c), it can be learned that a polarity of the taper (i.e. whether $W_d > 0$ or $W_d < 0$) does not affect the spring constants. For example, a beam with $W_c = 20$ μm and $W_e = 30$ μm will have the same spring constants with the one with $W_c = 30$ μm and $W_e = 20$ μm if all other geometries are equal. It is also learned that a beam taper rate W_d has an effect only to the linear spring constant k_1 whereas an average beam width W_a affects all spring constants. Ratios between a linear term and nonlinear terms of a spring can be controlled by adjusting h, W_a and W_d.

It is well established that a curved beam can feature bistable characteristics when its height h is higher than a certain critical value (h_{cr}). For a curved beam to have bistability, the equation $F_r(y_d) = 0$, must have three real roots. From equation (9), this condition leads to,

$$k_2^2 - 4k_1k_3 = 0 \qquad @\ h = h_{cr} \tag{11a}$$

$$\Rightarrow h_{cr} = \frac{4\sqrt{3}}{3}\left[W_a^2 + \left(1 + \frac{6}{\pi^2}\right)W_d^2\right]^{1/2}. \tag{11b}$$

For a non-tapered curved beam ($W_d = 0$), h_{cr} is reduced to $4W_a/\sqrt{3}$, which is found the same in literature [35]. Due to its importance, an initial curve height is often expressed in a unit of h_{cr}.

2.2. Tapered curved-beam hinge - numerical analysis

Next, spring constants of tapered curved beams were obtained via numerical analysis. More specifically, finite element analysis (FEA) was conducted to examine relationships between restoring force and beam center displacement (F_r-y_d) by using COMSOL Multiphysics® (version 5.2). Figure 2(a) illustrates an example of simulation results, showing distribution of elastic strain energy density when a certain amount of displacement is applied to a block at the beam center. Total elastic strain energy U stored in the beam is calculated by integrating the elastic strain energy density over the beam volume as presented in figure 2(b). Then, it is differentiated with respect to y_d to result in F_r (figure 2(c)). Figure 2(c) also includes analytically calculated F_r-y_d curves by using equation (9). Results by both methods show general agreement, exhibiting asymmetry about $y_d = 0$ and negative slopes for some regions in negative y_d. Quantitatively, some discrepancies are observed between two groups of results, which becomes more evident as h increases. One of the main reasons for such a discrepancy is attributed to limitation of the Galerkin method with one-mode approximation, used in development of the analytical model [36].

For the main analysis that will be described in section 2.3, spring constants were extracted from the FEA results. In order to do that, F_r-y_d graphs were fitted to third-order polynomials, as shown in figure 3(a). It shows that the fitting works relatively well for low beam heights. As the beam height increases (as can be seen when h is 1.5 h_{cr}), fitting error is substantial in the negatively sloped region. It should be noted, however, that these fitting errors do not affect the main analysis significantly because a negative slope implies that it is an unstable region, and also because the maximum power outputs were obtained mostly with low h values ($h < h_{cr}$, see figure 6). Examples of spring constants obtained through this procedure are presented in figure 3(b-d), as a function of beam height when $W_c = 20$ μm and $W_e = 40$ μm. The graphs also include the spring constants calculated analytically by using equations (10a–10c) for comparison. Once again, the spring constant versus beam height curves were fitted to second- or third-order polynomials, as indicated in figures 3(b)-(d), to be used in the main analysis (i.e. equation 13b).

Figures 3(e) and (f) show trends of nonlinearity as a taper rate W_d and a beam height h change. Figure 3(e) shows that quadratic-to-linear spring constant ratios (k_2/k_1) have maxima at certain beam heights. On the other hand, cubic-to-linear spring constant ratios (k_3/k_1) monotonically decrease as the beam height increases, as can

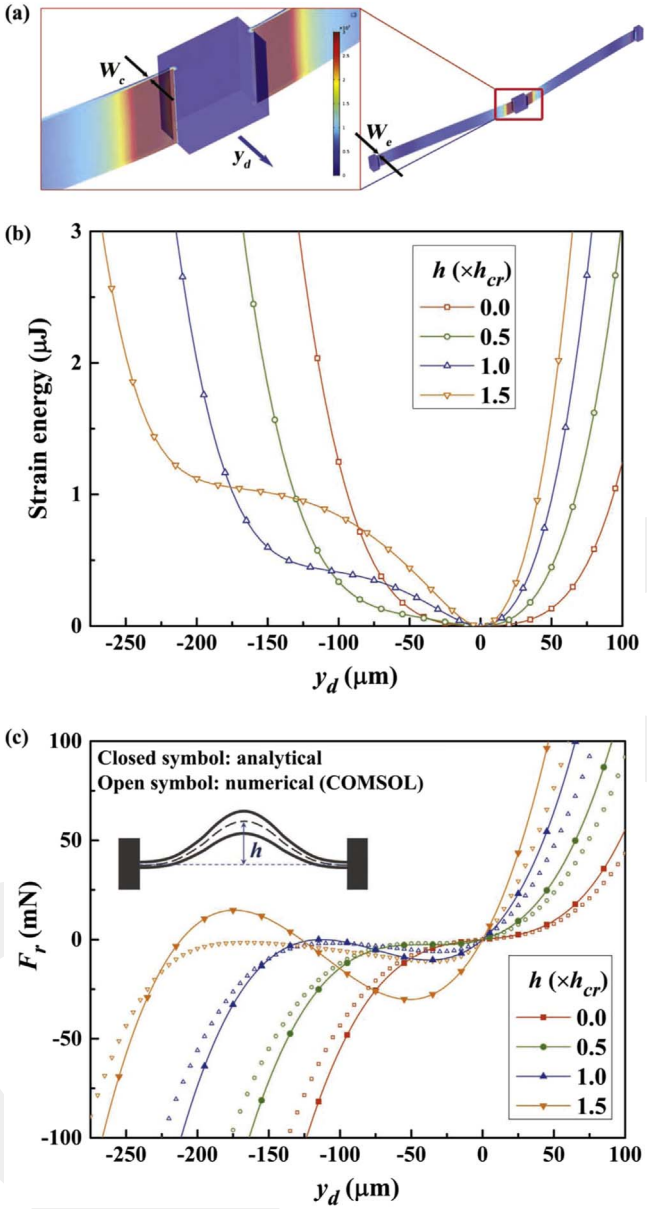

Figure 2. (a) An example of calculated elastic strain energy density (in J/m^3) distribution in a tapered curved beam under deformation. (b) Total elastic strain energy U stored in a beam as a function of y_d. $W_c = 20$ μm and $W_e = 40$ μm. (c) Restoring force F_r versus y_d. Open symbols: calculated from (b) via $\partial U/\partial y_d$; closed symbols: analytical from equation (9).

be seen from figure 3(f). It can be also learned that nonlinearity becomes weaker as a taper rate increases. Overall, figure 3 shows that the spring nonlinearity can be adjusted by means of a taper rate as well as a beam height.

2.3. Device model - stochastic differential equations

A model for the entire device was established by combining the mechanical part described in the previous subsection with an electrical part. As mentioned earlier, the electrical part of the VEH consists of two comb drives and an electret. This part can be modeled as two variable capacitors (C_A & C_B) and a voltage source (V_S) [19, 37]. V_S is associated with surface potential, i.e. initial charge of the electret. The model can be expressed by the following equations [19].

$$dV_A = \frac{1}{C_A + C_p}\left[(V_S - V_A)dC_A - \frac{V_A}{R_{LA}}dt\right] \tag{12a}$$

$$dV_B = \frac{1}{C_B + C_p}\left[(V_S - V_B)dC_B - \frac{V_B}{R_{LB}}dt\right] \tag{12b}$$

where V_A and V_B are the voltages on the loads R_{LA} and R_{LB}, respectively. C_p represents parasitic capacitance of the device.

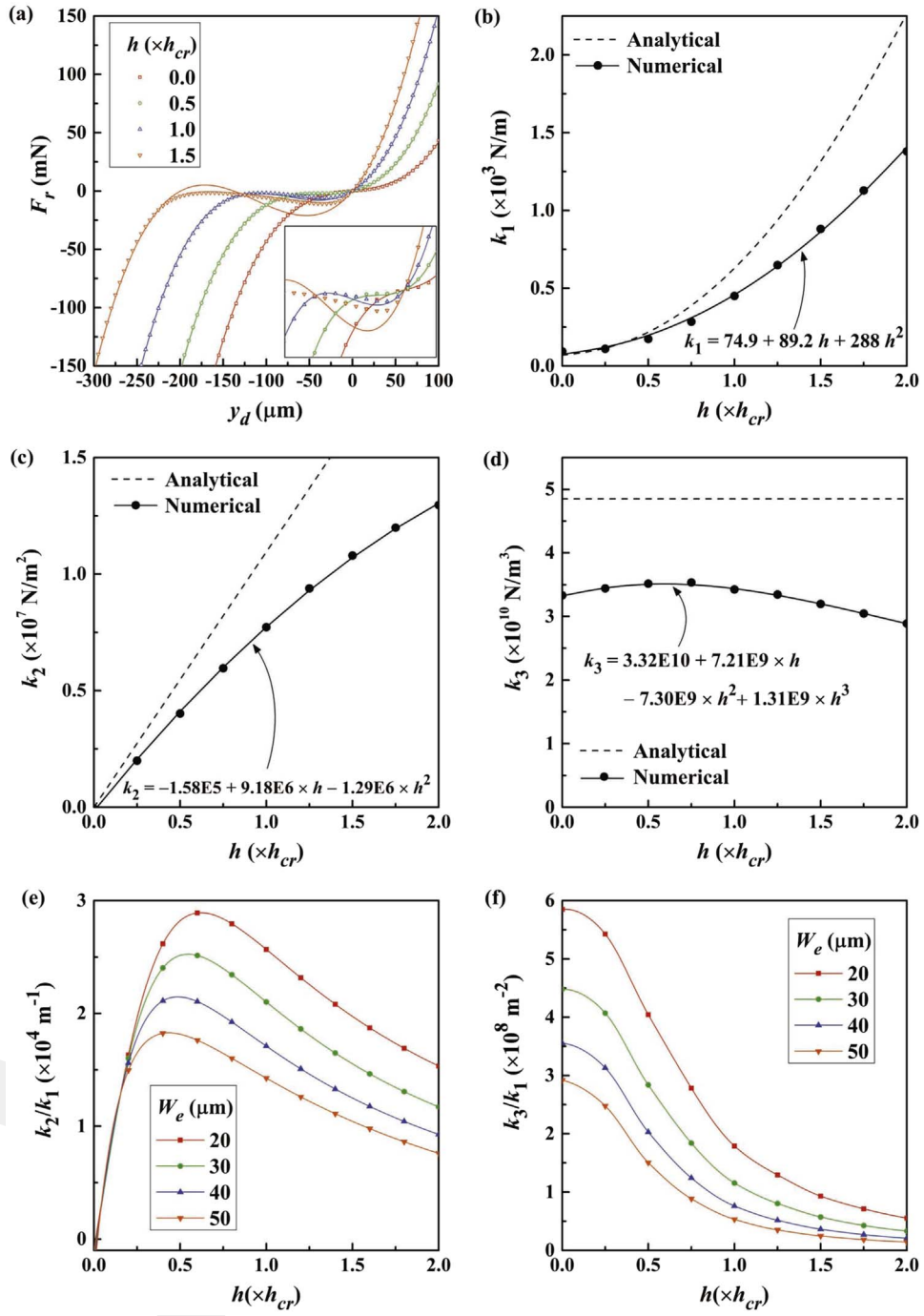

Figure 3. (a) F_r versus y_d. Symbols: COMSOL Multiphysics®. Lines: third-order polynomial fitting. Inset: magnified view near origin. (b) Linear, (c) quadratic, and (d) cubic spring constants. Symbols: polynomial fitting as in (a); solid lines: k_1, k_2, or k_3 fitted to polynomials as given in graphs; dashed lines: analytical. For (a-d), $W_c = 20\ \mu$m and $W_e = 40\ \mu$m. (e) Quadratic-to-linear and (f) cubic-to-linear spring constant ratios when $W_c = 20\ \mu$m.

The governing equations (stochastic differential equations) of the whole system can be summarized as follows [15].

$$dy_d = y_v dt \tag{13a}$$

$$dy_v = -\frac{1}{m}\left[c_d y_v + F_r(y_d) - \frac{1}{2y_v}\frac{dU_e}{dt}\right]dt + a_{ext}\,dt = y_a dt \tag{13b}$$

$$U_e = \frac{1}{2}[C_A(V_S - V_A)^2 + C_B(V_S - V_B)^2] \tag{13c}$$

Table 1. Device parameters and the nominal values used in the study.

Description (symbol)	Value	Description (symbol)	Value
Mass (m)	2.5 g	No. springs (N_s)	8
Damping coefficient (c_d)	1 g/s	Beam length (l)	8000 μm
Electret charging voltage (V_S)	200 V	Structure thickness (T)	400 μm
No. comb fingers (N_f)	900	Parasitic capacitance (C_p)	30 pF

$$a_{ext} = \frac{F_{ext}}{m} = \frac{\sigma}{m}\frac{dW_t}{dt} \tag{13d}$$

where m is a mass, y_v velocity of the mass, c_d a damping coefficient, U_e electrostatic potential energy, a_{ext} external acceleration, y_a acceleration of the mass, σ a diffusion coefficient that sets an input vibration strength, and W_t a Wiener process that models a stochastic vibration input. The beam center displacement y_d is the same as that of the mass.

2.4. Analysis methods

A Wiener process is a continuous-time stochastic process. Increment of a Wiener process, dW_t, is a Gaussian process with zero mean. To simulate a vibration input as colored noise, dW_t was generated in MATLAB® as a discrete time series, and processed through a low pass filter (cutoff @ 500 Hz). Then, this input time series was applied to equations (13a–13d). Spring constants of the tapered curved beams were obtained from the numerical simulation results as explained in section 2.2. The equations were solved by using the Euler-Maruyama method [38]. Root-mean-square (rms) power was calculated from the resulting voltage time series, and power spectral density (PSD) was computed by using fast Fourier transform (FFT). Two values of acceleration magnitude (a_{ext}, rms), i.e. 0.02g and 0.05g, were considered in this work, based on the study by Round *et al* [39]. In order to improve representativeness of the analysis results, simulation was repeated 500-2000 times for a single condition. The length of one time series was forty million, and a time step (dt) of 50 nanosecond was used. Table 1 summarizes the device parameters and their nominal values used in the simulation, most of which were taken from [28]. The value of a damping coefficient was determined by comparing the simulation results to the ones reported in [28]. For this comparison, a sinusoidal vibration input was used, as it was the input condition in the experiments by Honma *et al* [28]. Single-crystalline silicon (SCS) was considered as the main structural material. The beam widths considered (W_c & W_e) range from 20 μm to 50 μm. The lowest beam width value (20 μm) was determined in reference to the structure thickness (T: 400 μm), considering an aspect ratio that is reasonably achievable by dry etching in practice.

3. Results

Figure 4 presents examples of calculated time series. At a lower vibration strength ($a_{ext} = 0.02g$), the mass displacement y_d is shown symmetric about the idle position. In this condition, it can be deduced that the spring nonlinearity is not strongly in play. As dominant frequencies of the input change in time, the displacement magnitude changes in accordance with the spectral characteristics of the oscillator. The displacement waveform is much smoother than the input due to a mechanical (low pass) filtering effect. At a higher vibration strength ($a_{ext} = 0.05g$), the displacement becomes substantially asymmetric about the idle position, and variation in the envelope amplitude becomes significantly reduced. Both of these observations can be attributed to the spring nonlinearity, i.e. snap-through and spectrum broadening. At both vibration strengths, it is shown that the produced load current waveforms resemble those of the displacement.

Figure 5 presents effects of load resistances ($R = R_{LA} = R_{LB}$) to calculated average electric power outputs when a_{ext} is 0.05g. The results show that there exists an optimum load condition and an optimum beam height for a given beam taper parameter and at a given vibration strength. For example, when W_c is 20 μm and W_e is 30 μm, the optimum conditions are found as 20 MΩ and 0.95h_{cr} at 0.05g. In most of the cases considered in this study (except for the case of $W_c = W_e = 20$ μm), the optimum beam heights were found between 0 and 1h_{cr}. This finding can be connected to the k_2/k_1 ratios (figure 3(e)), which have the maxima within this range. In some conditions, e.g. $W_c = 20$ μm, $W_e = 30$ μm, and $R = 15$-25 MΩ (figure 5(a)), regions are found where P_{elec} drops in the middle. In other words, those curves have two peaks. The reason behind this phenomenon is not very clear at the moment. It is considered that the second peak is related to the bistability of a curved beam, judging from the observation that those peaks appear beyond $h = h_{cr}$. The optimum load conditions were found for each beam

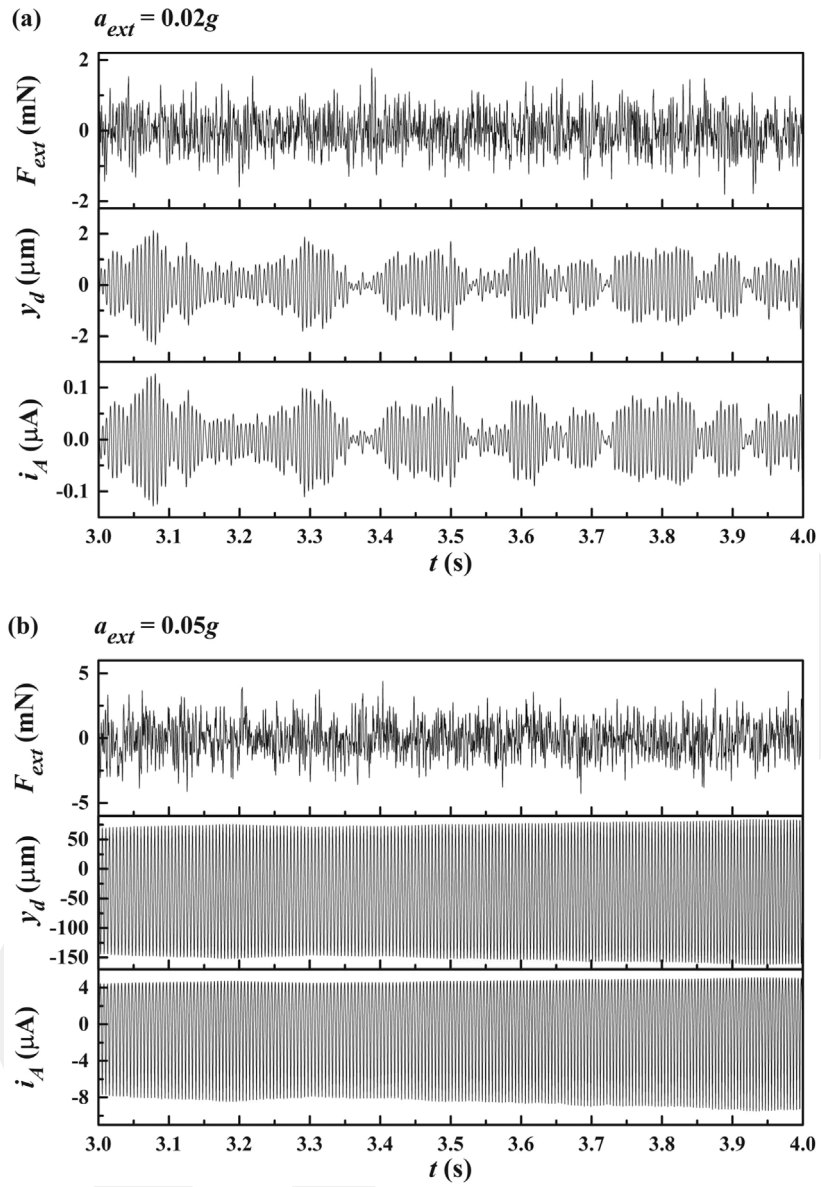

Figure 4. Examples of calculated time series (extracted from a length of eighty million). a_{ext}: (a) 0.02g and (b) 0.05g. i_A: current through a load R_{LA}. $W_c = 40$ μm, $W_e = 30$ μm, $R_{LA} = R_{LB} = 15$ MΩ and $h = 0.55h_{cr} = 45.18$ μm.

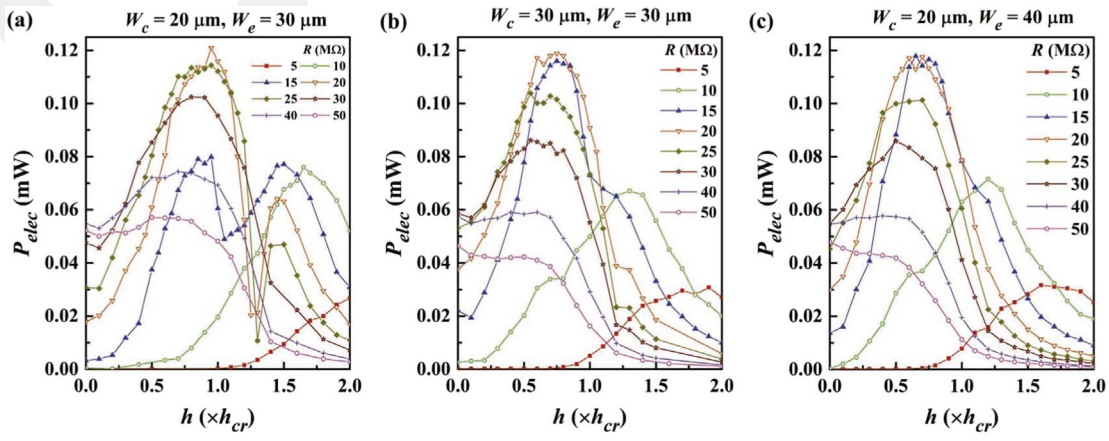

Figure 5. Calculated average electric power output P_{elec} at $a_{ext} = 0.05g$. Beam taper parameters (W_c, W_e): (a) 20 μm, 30 μm, (b) 30 μm, 30 μm, and (c) 20 μm, 40 μm. h_{cr}: (a) 59.56 μm, (b) 57.74 μm, and (c) 75.22 μm.

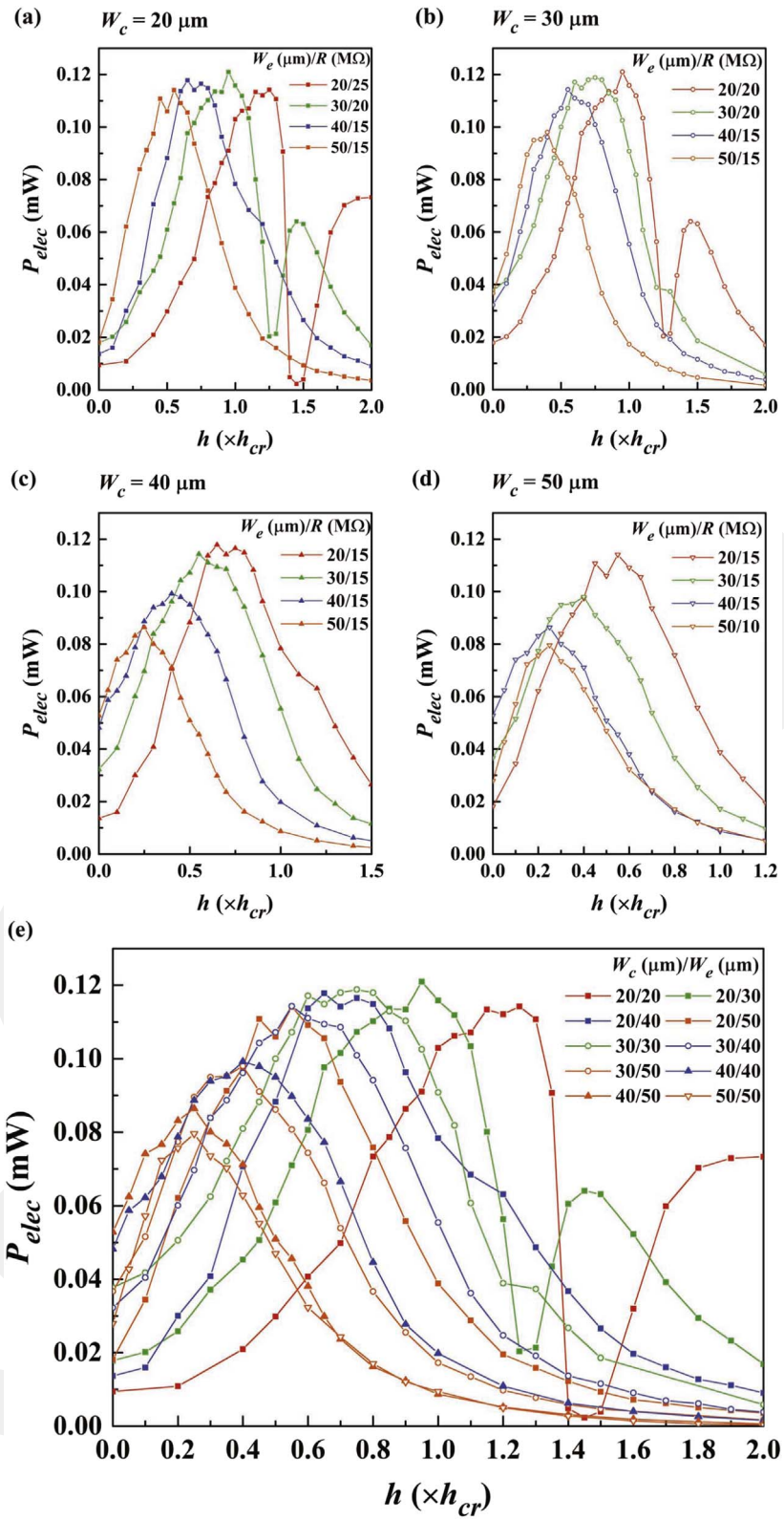

Figure 6. Calculated average electric power output P_{elec} at $a_{ext} = 0.05g$. Beam width at the center (W_c): (a) 20 μm, (b) 30 μm, (c) 40 μm, and (d) 50 μm. (e) Combined graph from (a) to (d). For each beam taper parameter set, only the results with the optimum load (R) values are shown.

taper parameter set (W_c & W_e), and the average electric power outputs with those load conditions are presented in figure 6.

When W_c is 20 μm (figure 6(a)), the highest electric power is obtained from W_e of 30 μm. As mentioned in section 2.1, the spring constants do not change when the values of W_c and W_e are interchanged. Therefore, the results for (W_c, W_e) = (30 μm, 20 μm) are the same as those for (W_c, W_e) = (20 μm, 30 μm) (see figures 6(a) and 6b). For W_c

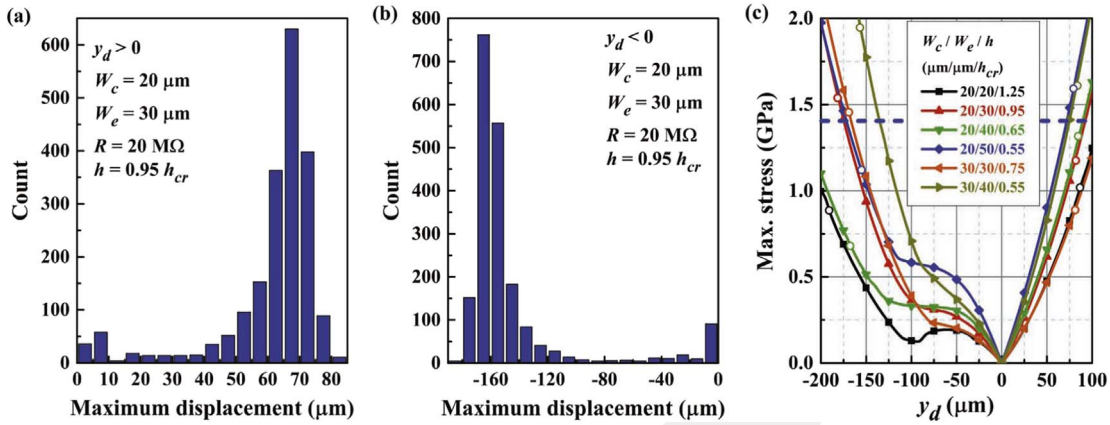

Figure 7. (a-b) Counts of maximum beam center displacements out of two thousand different simulation runs. Maximum displacements in (a) positive and (b) negative directions. $a_{ext} = 0.05g$. (c) Maximum von Mises stress versus y_d. Dashed line: silicon fracture strength (1.4 GPa); open circles: maximum displacements for specific beam parameters (table 2).

Table 2. Maximum beam center displacements (@ 0.05g) out of 2000 simulation runs and corresponding maximum von Mises stresses in both (positive and negative) directions. Stress values larger than the fracture strength of silicon (1.4 GPa) are indicated in bold. Average electric power outputs are also listed.

(W_c, W_e) [μm]/h[× h_{cr}]/R [MΩ]	Max. displ. [μm]		Max. stress [GPa]		Avg. power
	$y_d > 0$	$y_d < 0$	$y_d > 0$	$y_d < 0$	[μW]
(20, 20)/1.25/25	86.4	−191.1	1.02	0.89	114.2
(20, 30)/0.95/20	82.3	−182.1	1.18	**1.54**	121.0
(20, 40)/0.65/15	85.0	−166.8	1.33	0.68	117.8
(20, 50)/0.55/15	79.0	−156.1	**1.59**	1.12	114.1
(30, 30)/0.75/20	80.7	−169.5	0.89	**1.46**	118.8
(30, 40)/0.55/15	83.7	−156.8	**1.61**	**1.95**	114.2

of 30 μm (figure 6(b)), the best power is found at 20 μm of W_e. The same is true when W_c is 40 μm and 50 μm (figures 6(c) and 6d). Overall (figure 6e), the highest electric power of 121.0 μW is achieved with a (20 μm, 30 μm) combination of (W_c & W_e). This power output value is closely followed by the case of $W_c = W_e = 30$ μm with 118.8 μW (@$h = 0.75h_{cr}$) and the case of (20 μm, 40 μm) with 117.8 μW (@$h = 0.65h_{cr}$). It is intriguing to observe that the case of $W_c = W_e = 20$ μm (with the lowest spring constant values) does not result in the highest electric power output.

Another aspect worthy of examination in energy harvester operation is a stress level experienced by the beams. There are several (W_c, W_e) combinations producing similar average power outputs. However, stress levels they experience during operation are different from one another, even at the same vibration strength. This should be an important factor to be considered when final design selection is to be made. Beams need to be operated below the fracture strength at all times to prevent a damage. The fracture strength of single-crystalline silicon along {110} direction is reported to fall within the range between 1.4 GPa and 3.1 GPa [40]. As a conservative criterion, 1.4 GPa was selected as the limit in this study.

Six different sets of taper parameters were selected for a case study as summarized in table 2.

First, for each taper parameter, maximum displacements in both (positive and negative) directions were obtained out of 2000 time series. For example, figures 7(a) and 7(b) show distributions of the maximum displacements when $W_c = 20$ μm and $W_e = 30$ μm. In the positive direction (figure 7a), the most frequent occurrence of the maximum y_d is found to be between 65 μm and 70 μm while the highest value overall is 82.3 μm. This value is reported in table 2. In the negative direction, the largest displacement is found as −182.1 μm in this condition. In practice, it is the largest displacement that matters because if the stress induced at such a displacement goes beyond the fracture strength, a fracture can start from the beam. The largest displacements found for the six specific cases are summarized in table 2, and marked (with open circles) in figure 7(c).

Stress induced by beam deformation was investigated by using COMSOL Multiphysics® via the similar process used to calculate elastic strain energy density (figure 2a). For each beam center displacement (y_d), the highest von Mises stress was found from the simulation, as plotted in figure 7(c). The highest stress occurred at the junctions of hinges. Table 2 also provides the maximum von Mises stresses found at the largest displacements

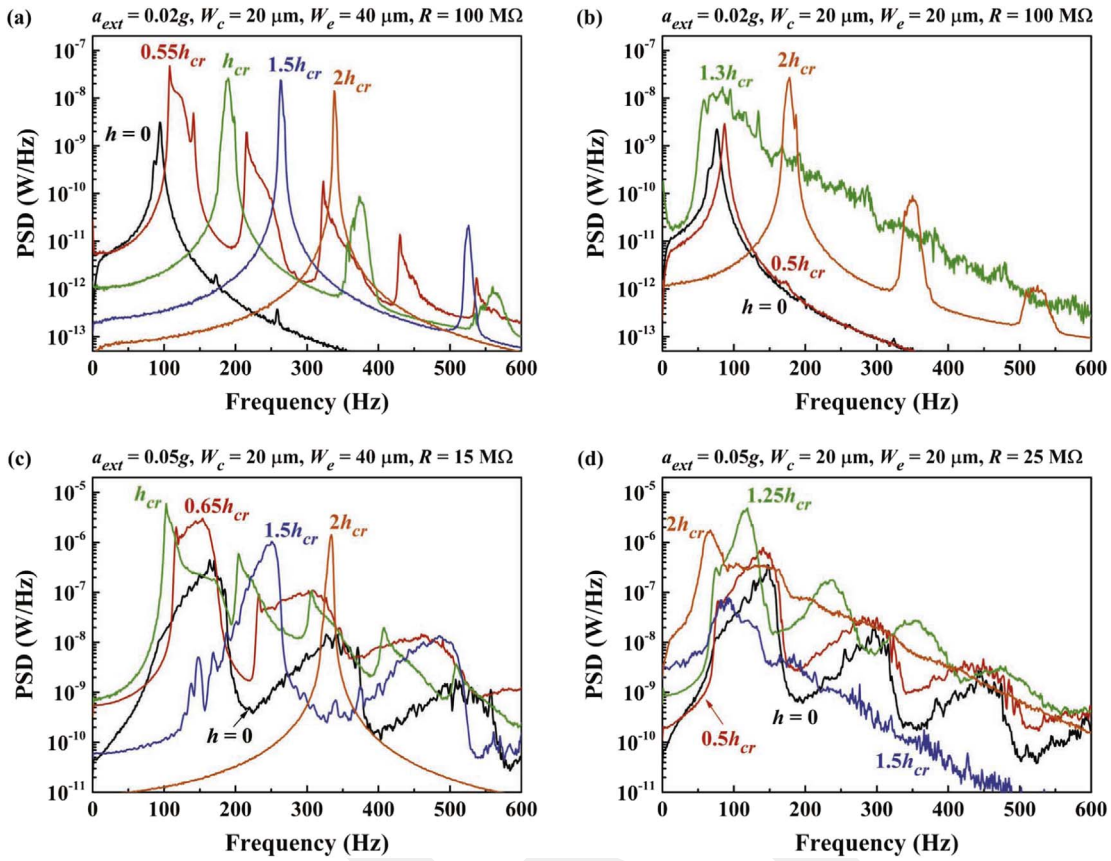

Figure 8. Calculated average electric power spectral density (PSD). The optimum beam heights are (a) $0.55h_{cr}$, (b) $1.3h_{cr}$, (c) $0.65h_{cr}$ and (d) $1.25h_{cr}$, respectively.

for each case when a_{ext} is 0.05g. For example, for (20 μm, 30 μm) combination, the maximum stress was found to be 1.54 GPa at the maximum displacement value of −182.1 μm. Out of 2000 simulation runs for this combination, in 34 times (i.e. 1.7%), the maximum displacement went beyond −175.3 μm, which corresponds to the maximum stress of 1.4 GPa. It was learned that out of six cases studied, only (20 μm, 20 μm) and (20 μm, 40 μm) combinations had the maximum stresses below the fracture strength (1.4 GPa) in both directions. For (20 μm, 30 μm) and (30 μm, 30 μm) combinations, the maximum stresses went beyond the fracture strength in negative y_d. For (20 μm, 50 μm) combination, it went over the fracture strength in positive y_d. For (30 μm, 40 μm) combination, the maximum stresses were larger than the fracture strength in both directions. When both the average electric power output and the maximum stress induced are considered, it can be concluded that (20 μm, 40 μm) combination is the best candidate at 0.05g, with 117.8 μW of average power output. This P_{elec} value is 3.2% higher than 114.2 μW of (20 μm, 20 μm) combination.

Figure 8 shows the power spectral density (PSD) of a tapered beam (20 μm, 40 μm combination) as well as a non-tapered beam ($W_c = W_e = 20$ μm) at two different vibration strengths and for various beam heights. At 0.02g (figures 8(a) and 8(b)), spectrum broadening is apparent only for limited ranges of h values, i.e. around $0.55h_{cr}$ for the (20 μm, 40 μm) combination and around $1.3h_{cr}$ for $W_c = W_e = 20$ μm. Narrow spectra are observed for both low h and high h values, resembling those of linear harmonic oscillators.

When compared to the (20 μm, 40 μm) combination with $h = 0.55h_{cr}$, the case of $W_c = W_e = 20$ μm with $h = 1.3h_{cr}$ shows a lower peak PSD value. Nevertheless, the spectrum broadening is quite substantial in the latter case, and as a result, higher maximum average power output is obtained compared to the former (figure 9). At 0.05g (figures 8(c) and 8d), ranges of h that exhibit spectrum broadening become significantly wider. The spectrum broadening can be observed even at $h = 0$. This spectrum broadening is the result of spring nonlinearity and the cause for substantial increase in power output at 0.05g.

Figure 9 presents calculated average electric power at a lower vibration strength ($a_{ext} = 0.02g$). Once again, it only includes the cases with the optimum load conditions. These optimum resistance values are higher compared to the cases when a_{ext} is 0.05g. At this vibration strength, a general trend is observed that the maximum power output as well as the optimum beam height decrease as the average beam width (W_a) increases. Hence, the highest electric power was obtained with the narrowest beam, i.e. $W_c = W_e = 20$ μm (it was different at 0.05g where it was not the narrowest W_a that produced the maximum power output). The highest electric

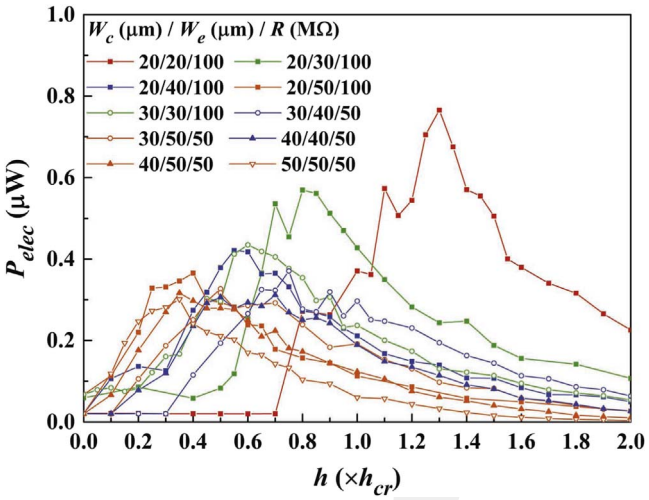

Figure 9. Calculated average electric power P_{elec}. For each beam taper condition, results with the optimum load (R) are included. $a_{ext} = 0.02g$.

power obtained is 0.77 μW at $h = 1.3h_{cr}$. At this vibration magnitude, the maximum displacements are found to be below 5 μm so that stresses incurred during operation are not of serious concern.

4. Discussion and conclusion

In this study, a curved-beam hinge with a linear lateral taper was explored as the spring component of an electret-based vibration energy harvester (eVEH). Nonlinear restoring force expression of the tapered curved beam was derived by considering relevant potential energy constituents, and the results were compared to those obtained via numerical simulation. By numerically solving stochastic differential equations that model the device, it was learned that higher electric power can be achieved with the tapered curved hinges in comparison to the non-tapered ones when the exerted acceleration has a magnitude (rms) of 0.05g. The maximum stress levels were investigated as well, which are expected to be experienced by tapered curved beams during operation. When the cases are excluded, of which maximum stresses go beyond the fracture strength of silicon, still it was found out that the tapered beam was the one that produces the highest power output. Therefore, it can be concluded that tapering of a curved-beam hinge can be a valuable addition for the design optimization of eVEHs. It is worth noting that addition of a lateral taper is not expected to incur any significant change in the device fabrication. It is also noteworthy to mention that due to the spring nonlinearity, the maximum achievable power increases dramatically (about 160 times instead of $2.5^2 = 6.25$ times) as a_{ext} increases from 0.02g to 0.05g.

As interest in vibration energy harvesting grow, broadening of the VEH spectra is anticipated to become more important in the foreseeable future. Among various ideas to pursue that purpose, nonlinear springs have a strong potential owing to requirement of minimal efforts in the device development. Future works include experimental validation of the proposed devices and further optimization of the curved beams including different beam shapes.

Acknowledgments

This work was partially supported by the Research Fund of Abdullah Gül University (FOA-2016-49).

Conflict of interest

The author declares that there are no known conflicts of interest to influence the work reported in this paper.

Data availability statement

All data that support the findings of this study are included within the article (and any supplementary files).

ORCID iDs

Dooyoung Hah https://orcid.org/0000-0002-1290-0597

References

[1] Jia Y 2020 *J. Intell. Mater. Syst. Struct.* **31** 921–44
[2] Iqbal M, Nauman M M, Khan F U, Abas P E, Cheok Q, Iqbal A and Aissa B 2021 *Int. J. Energy Res.* **45** 65–102
[3] Prajwal K T, Manickavasagam K and Suresh R 2022 *Eur. Phys. J.: Spec. Top.* **231** 1359–71
[4] Zhou S, Lallart M and Erturk A 2022 *J. Sound Vib.* **528** 116886
[5] Erturk A, Hoffmann J and Inman D J 2009 *Appl. Phys. Lett.* **94** 254102
[6] Sebald G, Kuwano H, Guyomar D and Ducharne D 2011 *Smart Mater. Struct.* **20** 102001
[7] Liu H, Zhao L, Chang Y, Shan G and Gao Y 2022 *Int. J. Mech. Sci.* **223** 107291
[8] Li X, Yu K, Upadrashta D and Yang Y 2019 *Smart Mater. Struct.* **28** 035010
[9] Saxena S, Dwivedi R K and Khare V 2021 *Appl. Phys. A* **127** 798
[10] Ahmad M M, Khan N M and Khan F U 2022 *Sens. Actuators A* **344** 113690
[11] Lien I C, Lo Y C, Chiu S H and Shu Y C 2022 *J. Mech.* **38** 518–30
[12] Zhang B, Li H, Zhou S, Liang J, Gao J and Yurchenko D 2022 *Mech. Syst. Signal Process.* **176** 109169
[13] Mollik T, Geng Y, Shougat M R E U, Fitzgerald T and Perkins E 2022 *Heliyon* **8** e11833
[14] Hajati A and Kim S G 2011 *Appl. Phys. Lett.* **99** 083105
[15] Ando B, Baglio S, L'Episcopo G and Trigona C 2012 *J. Microelectromech. Syst.* **21** 779–90
[16] Scerri J, Grech I, Gatt E and Casha O 2015 *Electron. Lett.* **51** 409–11
[17] Du H, Chau F S and Zhou G 2018 *J. Microelectromech. Syst.* **27** 34–9
[18] Nguyen S D, Halvorsen E and Paprotny I 2013 *Appl. Phys. Lett.* **102** 023904
[19] Hah D 2023 *J. Intell. Mater. Syst. Struct.* **34** 1702–12
[20] Leadenham S and Erturk A 2014 *J. Sound Vib.* **333** 6209–23
[21] Chen K, Ding X, Tian L, Shen H, Song R, Bian Y and Yang Q 2023 *Mech. Syst. Signal Process.* **188** 110066
[22] Ghasemi S, Afrang S, Rezazadeh G, Darbasi S and Sotoudeh B 2020 *Microsyst. Technol.* **26** 2389–98
[23] Xu R, Akay H and Kim S G 2019 *Research* **2019** 1087946
[24] Zou D, Liu G, Rao Z, Tan T, Zhang W and Liao W H 2021 *Mech. Syst. Signal Process.* **153** 107526
[25] Chen Z and Chen F 2023 *Nonlinear Dyn.* **111** 4121–39
[26] Pan D, Liang Y, Zhang Z and Wu Z 2025 *Mech. Syst. Signal Process.* **224** 112013
[27] Honma H, Mitsuya H, Hashiguchi G, Fujita H and Toshiyoshi H 2018 *J. Micromech. Microeng.* **28** 064005
[28] Honma H, Tohyama Y and Toshiyoshi H 2019 *20th Int. Conf. Solid-State Sens. Actuators and Microsyst. & Eurosensors XXXIII (Berlin, Germany)* 362–5
[29] Hashiguchi G and Toshiyoshi H 2023 *Sens. Mater.* **35** 1957–83
[30] Reddy G K, Singh P, Ravi K C, Anusha B, Gowri C and Vivek R 2024 *J. Phys.: Conf. Ser.* **2837** 012104
[31] Casals-Terre J, Fargas-Marques A and Shkel A M 2008 *J. Microelectromech. Syst.* **17** 1082–93
[32] Lacarbonara W, Nayfeh A H and Kreider W 1998 *Nonlinear Dyn.* **17** 95–117
[33] Rezaei H D A, Kadkhodaei M and Nahvi H 2012 *J. Intell. Mater. Syst. Struct.* **23** 1107–17
[34] Simitses G J 1990 *Dynamic Stability of Suddenly Loaded Structures* (Springer-Verlag) 117
[35] Qiu J, Lang J H and Slocum A H 2004 *J. Microelectromech. Syst.* **13** 137–46
[36] Zhang Y, Huang K and Xu W 2023 *Buildings* **13** 2645
[37] Yang Z, Tang L, Tao K and Aw K C 2019 *Int. J. Precis. Eng. Manuf. - Green Technol* **8** 113–23
[38] Kloeden P and Platen E 1995 *Numerical Solution of Stochastic Differential Equations* (Springer-Verlag) 305
[39] Roundy S, Wright P K and Rabaey J 2003 *Comput. Commun.* **26** 11311144
[40] Wilson C J and Beck P A 1996 *J. Microelectromech. Syst.* **5** 142–50